Single-Phase On-Board Integrated Battery Chargers for EVs Based on Multiphase Machines

Ivan Subotic, *Student Member, IEEE*, Nandor Bodo, and Emil Levi, *Fellow, IEEE*

***Abstract*—The paper considers integration of multiphase (more than three phases) machines and converters into a single-phase charging process of electric vehicles (EVs) and, thus, complements recently introduced fast charging solutions for the studied phase numbers. One entirely novel topology, employing a five-phase machine, is introduced and assessed jointly with three other topologies that use an asymmetrical nine-phase machine, an asymmetrical six-phase machine, and a symmetrical six-phase machine. In all topologies, both charging and vehicle-to-grid (V2G) mode are viable. Moreover, all are capable of unity power factor operation. A torque is not produced in machines during charging/V2G process so that mechanical locking is not required. Hardware reconfiguration between propulsion and charging/V2G mode is either not required or minimized by using a single switch. Theoretical analysis of operating principles is given, and a control scheme, applicable to all topologies and which includes current balancing and interleaving strategy, is developed. Finally, operation of all topologies is compared by means of experiments in both charging and V2G mode, with a discussion of influence of current balancing and interleaving strategy on the overall performance.**

***Index Terms*—Battery chargers, electric vehicles (EVs), integrated on-board chargers, multiphase machines.**

I. Introduction

ELECTRIC vehicles (EV) drivetrain and charging equipment are never used simultaneously. This allows integration of drivetrain power electronics, primarily an electric machine and an inverter, into the charging process, as an alternative to nonintegrated wired or wireless battery charging [1], [2]. The accomplishments of the integration are savings on cost, weight and space in the vehicle. Although three-phase machines are a preferable choice for propulsion [3], they cannot be easily integrated into fast (three-phase) charging process. The major obstacle is that a rotating field gets produced when three-phase currents flow through the machine. This demands various techniques in order to avoid torque production [4]–[6], which always include additional nonintegrated elements. Hence, the cost and complexity of the system are increased.

Manuscript received June 9, 2015; revised September 15, 2015; accepted November 14, 2015. Date of publication November 30, 2015; date of current version March 25, 2016. This work was supported by the Engineering and Physical Sciences Research Council (EPSRC) under Project EP/I038543/1 [Vehicle Electrical Systems Integration (VESI)]. Recommended for publication by Associate Editor S. Choi.

I. Subotic was with the School of Engineering, Technology, and Maritime Operations, Liverpool John Moores University, Liverpool, L3 3AF, U.K. He is now with ETH Zurich, 8092 Zurich, Switzerland. (e-mail: ivansubotic86@gmail.com).

N. Bodo and E. Levi are with the School of Engineering, Technology, and Maritime Operations, Liverpool John Moores University, Liverpool, L3 3AF, U.K. (e-mail: n.bodo@ljmu.ac.uk; e.levi@ljmu.ac.uk).

Color versions of one or more of the figures in this paper are available online at http://ieeexplore.ieee.org.

Digital Object Identifier 10.1109/TPEL.2015.2504400

On the other hand, multiphase machines are not characterized with these problems. They have additional degrees of freedom that can be utilized to transfer excitation (or a part of it) from the first (torque-producing) into other (passive) planes that do not yield torque production. At present, a nine-phase machine [7], an asymmetrical six-phase machine, a symmetrical six-phase machine [8]–[11], and a five-phase machine [12] have been proposed for integration into fast three-phase charging process. Topology of [13], which uses the machine as a three-phase one in propulsion mode, is also based on, in essence, a symmetrical six-phase machine in the charging/V2G mode.

Unlike three-phase chargers, single-phase chargers are only capable of slow charging. Nevertheless, if an EV is already equipped with a fast integrated three-phase charger, single-phase charger can complement it and serve as a great asset due to the wide spread of single-phase mains. Therefore, it is essential to provide single-phase charging option in addition to the fast three-phase integrated charging. Various proposals for integration of a three-phase machine into single-phase charging process already exist [14]–[18]. Compared to integrated chargers with multiphase machines, discussed here, they provide comparable performances. However, as already noted, integration of a three-phase machine into a three-phase charging process demands additional nonintegrated elements in order to avoid torque production. Therefore, in what follows the focus is on integrated single-phase chargers employing machine types that can also be easily integrated into three-phase charging process, namely, multiphase machines.

In the past, integration of a six-phase machine into a single-phase charging process received a lot of attention. It is patented in [19] and considered at a simulation level in [20] and [21]. Current balancing between phases of the same set is not considered, and experimental results are not provided. However, experimental results are available for a similar case of a set of two three-phase machines [22]. In [23], the integration of a nine-phase machine into a single-phase charging process is proposed at a theoretical level. Only basic control with simulation results is provided, and there are no experimental results. Until now, integration of a five-phase machine into a single-phase charging process has not been considered at all.

This paper provides an extensive analysis of single-phase chargers incorporating: an asymmetrical nine-phase machine, an asymmetrical six-phase machine, a symmetrical six-phase machine, and a five-phase machine. It is important to emphasize that, for each considered multiphase topology, a corresponding fast charging (three-phase) scheme has already been developed. Hence, the paper complements the work described in [7] for a nine-phase machine; in [10], for six-phase machines

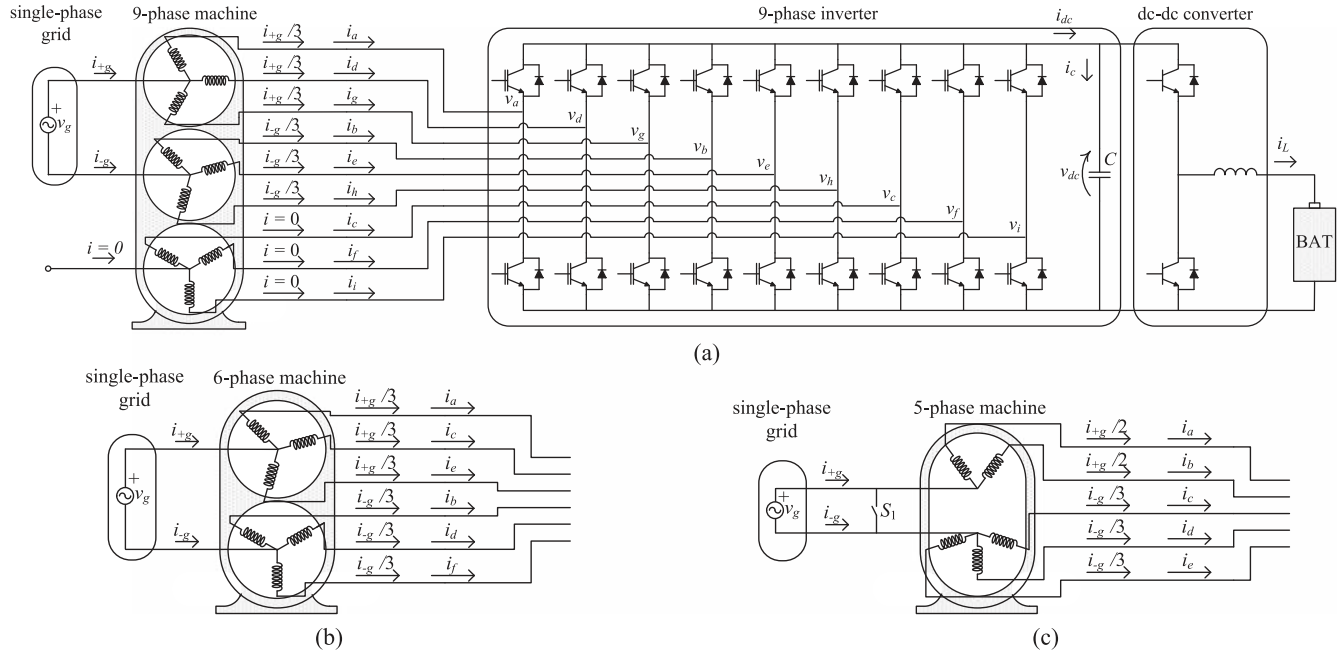

Fig. 1. Topologies of integrated single-phase battery chargers employing: (a) a nine-phase machine, (b) a six-phase machine, and (c) a five-phase machine.

(asymmetrical and symmetrical); and in [12], for a five-phase system architecture, all enabling fast charging with zero average torque production and full integration of the machine and the power electronic converter into the charging/V2G process. In simple terms, solutions of [7], [10], and [12], when combined with the topologies and control schemes described in this paper, give simultaneously means for achieving both slow and fast battery charging for a given phase number. In this paper, a two-level multiphase inverter is used at all times. However, the operating principles are equally applicable to corresponding systems based on three-level inverters, which are currently considered for use in future EVs [24], [25].

The paper is organized as follows. In Section II, a theoretical analysis of the charging process and operating principles is given. The complete control algorithm, including the current balancing and interleaving strategy, is presented in Section III and is valid, with minor variations, for all the considered topologies. In Section IV, experimental results for charging and V2G modes are given for all four considered cases and the influence of current balancing and interleaving strategies on the performance is discussed. Section V provides preliminary efficiency evaluation of the charging/V2G process, while Section VI concludes the paper.

II. Theoretical Analysis

The investigated topologies are presented in Fig. 1. A dc–dc converter, shown on the right-hand side of Fig. 1(a), may or may not be required, depending on the battery and grid voltage levels. Its presence or absence has no impact on the principles of operation of the considered topologies, and similar to [7], [10], and [12], it is not used in the experimental setup. Meeting safety regulations with nonisolated charging could be achieved by various techniques, one of which is described in [26].

TABLE I
Correlations Between Machines' and Grid Currents

Topology	Correlations
Fig. 1(a)	$i_a = i_d = i_g = i_{+g}/3 \quad i_b = i_e = i_h = i_{-g}/3$ $i_c = i_f = i_i = 0$
Fig. 1(b)	$i_a = i_c = i_e = i_{+g}/3 \quad i_b = i_d = i_f = i_{-g}/3$
Fig. 1(c)	$i_a = i_b = i_{+g}/2 \quad i_c = i_d = i_e = i_{-g}/3$

In integrated chargers employing a nine-phase machine [either asymmetrical or symmetrical, see Fig. 1(a)], an asymmetrical six-phase machine, and a symmetrical six-phase machine [see Fig. 1(b)], the grid is connected directly between the two machine's neutral points. Therefore, a hardware reconfiguration is not required between propulsion and charging/V2G operation. On the other hand, the integrated charger employing a five-phase machine requires hardware reconfiguration. For the charging/V2G mode switch S_1, which forms the neutral point of the machine in the propulsion mode, has to be opened [see Fig. 1(c)].

The machines' behavior in charging and V2G modes can be assessed by considering the decoupling transformation (Clarke's) matrices. For this purpose, equal current sharing between machine phases connected to the same grid terminal is assumed. Decoupling matrices for asymmetrical nine- and six-phase machines can be found in [7] and [11], respectively, while for symmetrical six-phase and five-phase machines, they are given in [27].

Grid currents are in all topologies governed by

$$i_{+g} = \sqrt{2} I \cos(\omega t), \qquad i_{-g} = -\sqrt{2} I \cos(\omega t). \tag{1}$$

Simple observation of connections from Fig. 1(a)–(c) is sufficient in order to determine correlations between machines'

TABLE II
EXCITATION MAPPING INTO MACHINES' PLANES

Topology	Excitation in Torque Producing Plane	Excitation in Nontorque Producing (Passive) Plane(s)	Excitation of Zero Sequence
Fig. 1(a)	$\underline{i}_{\alpha\beta} = 0$	$\underline{i}_{x1y1} = I(0.33 - j0.577)\cos(\omega t)$ $\underline{i}_{x2y2} = 0$ $\underline{i}_{x3y3} = 0$	$i_0 = (\sqrt{8}/3)I\cos(\omega t)$
Fig. 1(b) (asymmetrical)	$\underline{i}_{\alpha\beta} = 0$	$\underline{i}_{xy} = 0$	$i_{0-} = -\sqrt{6}(I/3)\cos(\omega t)$ $i_{0+} = \sqrt{6}(I/3)\cos(\omega t)$
Fig. 1(b) (symmetrical)	$\underline{i}_{\alpha\beta} = 0$	$\underline{i}_{xy} = 0$	$i_{0-} = (\sqrt{12}/3)I\cos(\omega t)$ $i_{0+} = 0$
Fig. 1(c)	$\underline{i}_{\alpha\beta} = (0.9757 + 0.7089j) \cdot I \cdot \cos(\omega t)$	$\underline{i}_{xy} = (0.1424 + 0.4381j) \cdot I \cdot \cos(\omega t)$	$i_0 = 0$

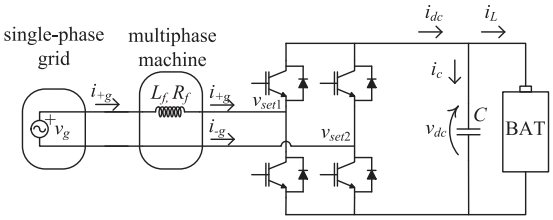

Fig. 2. Equivalent charging/V2G scheme (without a dc–dc converter).

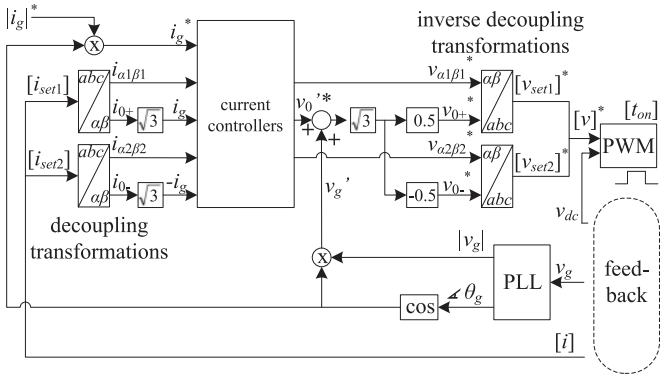

Fig. 3. Control algorithm for the single-phase charging/V2G mode.

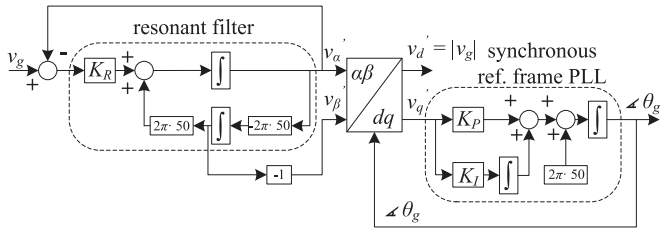

Fig. 4. Single-phase PLL algorithm.

currents and grid currents in all topologies. The correlations are summarized in Table I. It should be noted that correlations related to Fig. 1(b) are valid both for asymmetrical and symmetrical six-phase topologies.

By taking into account (1), substitution of correlations from Table I into decoupling matrices for asymmetrical nine-phase, asymmetrical six-phase, symmetrical six-phase, and five-phase topologies (available in [7], [11], and [27]) provides information on excitation mapping into machines' planes. The results are summarized in Table II. Derivation of results given in Table II is illustrated in Appendix I.

From Table II, it can be seen that for an asymmetrical nine-phase topology, an asymmetrical six-phase topology, and a symmetrical six-phase topology, the first plane is without excitation. The whole excitation is transferred into the second plane and/or zero-sequence component(s), none of which is capable of torque production. In these topologies, there is no field production in the rotor and machines' act as sets of passive components. As there is no field production in the rotors, machines' stator resistance and leakage inductance play a role of a current filter.

On the other hand, in the five-phase topology, the first plane is excited (see Table II). However, the excitation pulsates along single direction (spatially shifted from phase *a* axis by 36°). Therefore, it is incapable of producing a torque. Hence, the machine naturally stays at standstill during the charging process, and does not have to be mechanically locked. Thus, similarly as in the previous cases, the machine can be observed as a set of passive components. This fact is of great importance for the control algorithm, as it allows a great simplification of the machines' equivalent model during charging/V2G process, which is considered in the next section.

III. CONTROL ALGORITHM

The equivalent scheme of single-phase chargers utilizing multiphase machines is relatively straightforward. From Section II, it follows that machines in this process act as pure resistive–inductive elements. The chargers' equivalent scheme is given in Fig. 2. While in a physical system both terminals of a single-phase grid are attached to machine phases, in Fig. 2 machine parameters from both grid branches are lumped together. Thus, the filter L_f, R_f in Fig. 2 consists of a series connection of two *R–L* elements and has the value of their sum. The resulting scheme is a well-known single-phase full-bridge converter. It is applicable to all topologies of Fig. 1, and the difference may only appear in the *R–L* parameters of the filter.

The control algorithm for the single-phase full-bridge converter of Fig. 2 is given in Fig. 3. Measurements of grid and dc-bus voltage and machine currents are required. The grid voltage position is found by a single-phase phase-locked loop (PLL), shown in Fig. 4. It differs from the one for three-phase systems [7], [10] because there is no decoupling transformation applied to the grid voltages. An additional difference when compared to three-phase systems is that rotational transformations are not applied to machine currents. As it is shown in what follows, unlike in three-phase systems, α–β current components are

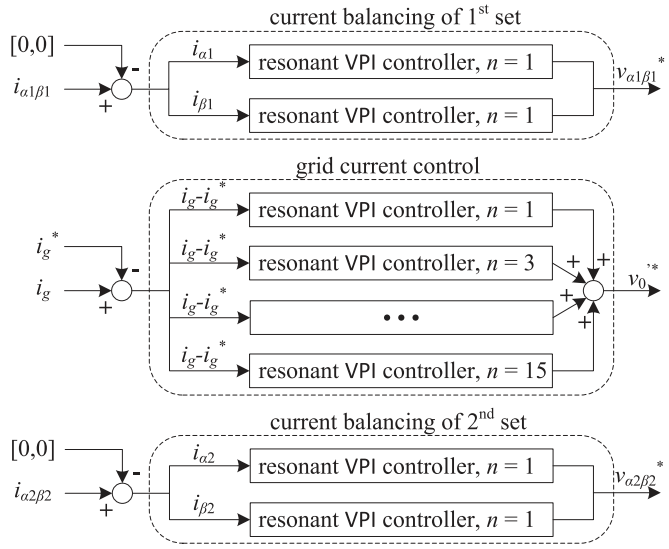

Fig. 5. Current controllers.

kept at zero, while zero-sequence current is utilized for energy transfer.

The input of the system is a reference for the current amplitude $|i_g|^*$. The reference could be obtained as an output of a battery charging current controller or dc-bus voltage controller. It should be multiplied by a sine function in order to obtain phase current reference. In order to achieve unity power factor, that sinewave should follow the phase of the grid current. In Fig. 3, it is obtained from grid voltage position angle θ_g by finding its cosine. The resulting sinusoid has two functions. When multiplied with the grid current amplitude reference $|i_g^*|$, the reference i_g^* for the grid current is obtained. The other function is that, if multiplied with the grid voltage amplitude $|v_g|$, from PLL, it produces filtered grid voltage signal v_g. This signal is then summed with the output of the current controller block $v_0'^*$ in order to prevent high current at the start-up of the charging process.

A. Grid Current Control

Although only two inverter legs are shown in Fig. 2, they represent sets of legs working in parallel. Therefore, an additional sensor for measuring grid current can be avoided by obtaining this information from sensors of paralleled inverter legs. In Fig. 3, this is accomplished by finding the zero-sequence component of currents belonging to the same set.

The subsequent multiplication with $\sqrt{3}$ is required only if power invariant three-phase decoupling transformation is utilized.

When grid current i_g is obtained either from the first or the second set (information from the other set is disregarded), it is controlled to its reference i_g^* in the block "current controllers." The block is shown in detail in Fig. 5, and its middle part is utilized for this purpose. Unlike in standard drives, it can be seen that the reference is subtracted from the measured current. It is a consequence of the fact that when inverter voltage increases the charging current decreases and vice versa. The difference is then fed into resonant vector proportional–integral (VPI) controllers.

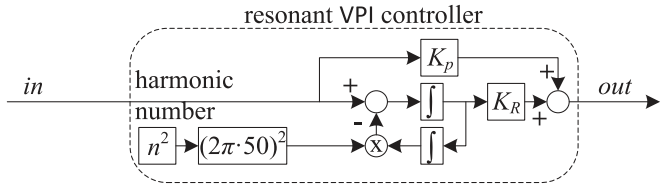

Fig. 6. Resonant VPI controller (n denotes the harmonic number).

They have the same form as in [7], [10], which is shown in Fig. 6. Each controller zeroes the current component at the frequency to which it is tuned. Therefore, the first one in Fig. 5, with $n = 1$ (fundamental frequency) controls the grid current fundamental.

However, grid current also contains odd low-order harmonics, caused by converter dead time. Thus, the control should compensate all odd low-order harmonics produced by the converter dead time. These are predominantly the 3rd, 5th, 7th, 9th, 11th, 13th, and 15th. Unlike in systems with three-phase supply, all odd harmonics are present. Each of these harmonics can be controlled by a resonant VPI controller that is tuned to a specific harmonic that it attempts to eliminate. Conveniently, these controllers can be placed in parallel in order to suppress a wide range of harmonics. In Fig. 5, it is shown how the parallel connection of resonant VPI controllers zeroes all harmonics up to the 15th. It should be noted that harmonics even higher than 15th can be controlled in the same manner. However, the control up to 15th harmonic is chosen here since it is believed to provide satisfactory results. Signal $v_0'^*$ is obtained by summing controllers' outputs.

Sum of signals $v_0'^*$ and v_g' is multiplied by $\sqrt{3}$ (see Fig. 3), in order to cancel the effect of power invariant inverse decoupling transformations. The modulation strategy is application of the same carriers and mutually inverse modulation signals to the two sets of phases; thus, factors 0.5 and -0.5 are utilized. Finally, after inverse decoupling transformations, voltage references for both sets are obtained. They enter the pulsewidth-modulation (PWM) unit, which has the same form as for the propulsion mode, only without zero-sequence injection.

B. Current Balancing

The control described in the previous section is sufficient if machine phases have identical impedances to current flow. Then, by placing machine phases (of the same set) in parallel, it is accomplished that the same currents flow through them. However, in practice, ideal symmetry is never the case. This results in higher currents in phases with lower equivalent impedances and causes slight phase shifts between currents belonging to the same set. Since machine currents are no longer in phase, there is an increased risk of a torque production. In order to avoid these problems, performing current balancing is essential.

The set imbalance manifests through appearance of α–β components of the current in the machine. These are separated from the useful (zero sequence, i.e., grid) current by means of two decoupling transformations (see Fig. 3). Once isolated, they are controlled to zero by resonant VPI current controllers, shown in Fig. 5, under the name "current balancing of 1st/2nd set." Only fundamental component is controlled.

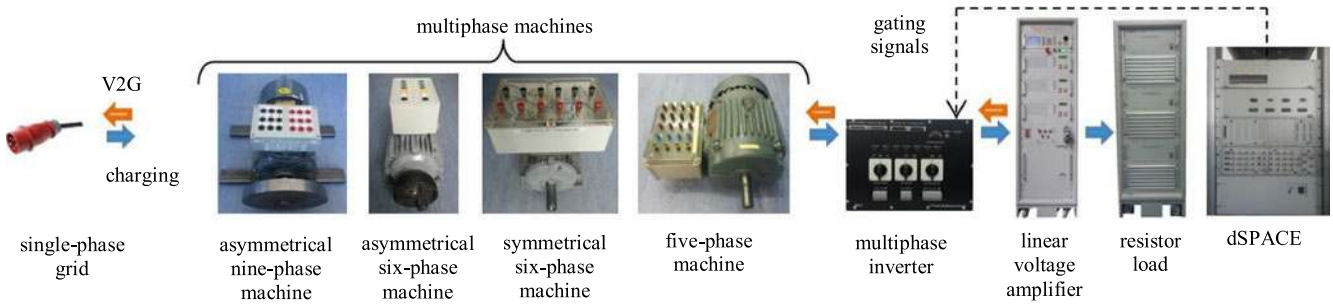

Fig. 7. Experimental rig.

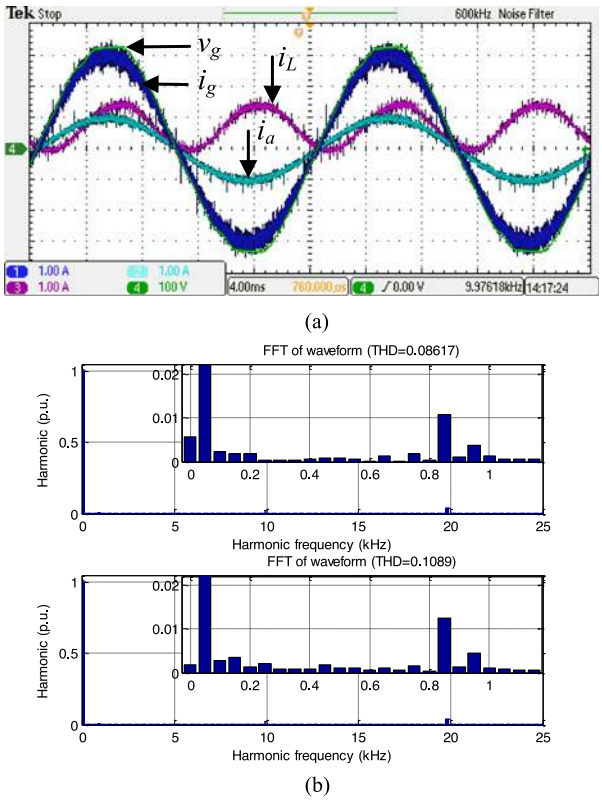

Fig. 8. Nine-phase machine in charging mode: (a) grid voltage v_g, grid current i_g, machine current i_a, and battery charging current i_L; (b) spectra of grid current i_g (upper graph) and machine current i_a (lower graph).

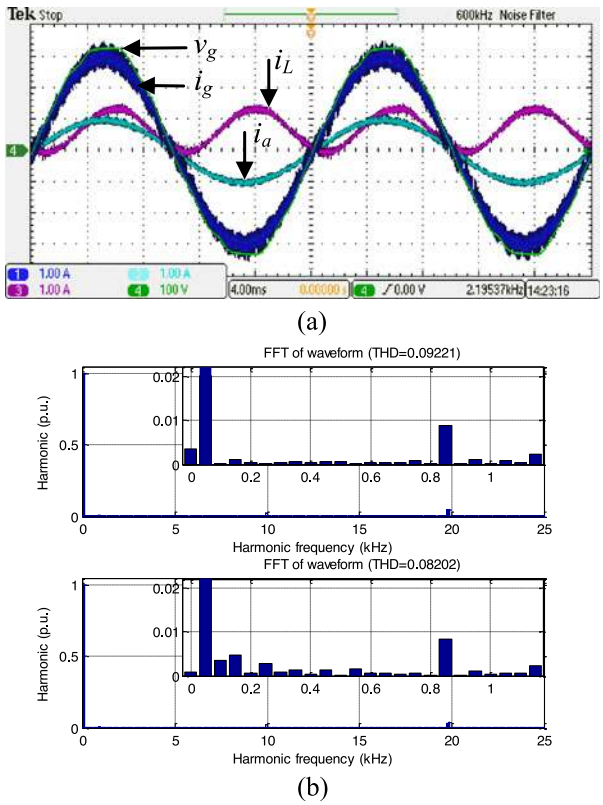

Fig. 9. Asymmetrical six-phase machine in charging mode: (a) grid voltage v_g, grid current i_g, machine current i_a, and battery charging current i_L; (b) spectra of grid current i_g (upper graph) and machine current i_a (lower graph).

It should be noted that charger employing a five-phase machine [see Fig. 1(c)] requires a slightly modified control. While the control of the second set is identical as elaborated above, the first set has only two phases. Therefore, a decoupling matrix should have the form of

$$[C] = \sqrt{\frac{1}{2}} \begin{bmatrix} 1 & -1 \\ 1 & 1 \end{bmatrix}. \tag{2}$$

Now, the first component represents the difference of the two currents, and it should be controlled to zero. Unlike in the previous cases (where two controllers were required), it can be accomplished with single resonant VPI controller, tuned to the first harmonic. The second component represents scaled grid current, and this information can be disregarded since the same information is obtained from the second set.

Outputs of balancing current controllers ($v_{\alpha 1 \beta 1}{}^*$ and $v_{\alpha 2 \beta 2}{}^*$), together with outputs of grid current controllers ($v_{0+}{}^*$ and $v_{0-}{}^*$), enter the inverse decoupling transformations and create final voltage references for each set ($[v^*_{\text{set}1}]$ and ($[v^*_{\text{set}2}]$), Fig. 3. A final remark is that, if a five-phase machine is used, the factor of 0.5 in front of the first inverse decoupling transformation should be multiplied with $\sqrt{2/3}$, since a different inverse decoupling matrix is used [transpose of (2)].

C. Interleaving Strategy

The single-phase charging topologies employing multiphase machines have an additional advantage that can facilitate

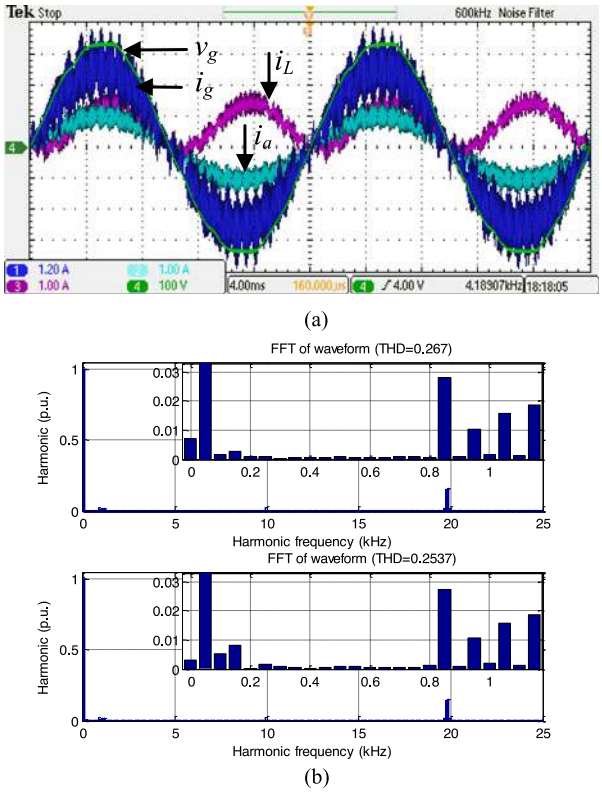

Fig. 10. Symmetrical six-phase machine in charging mode: (a) grid voltage v_g, grid current i_g, machine current i_a, and battery charging current i_L; (b) spectra of grid current i_g (upper graph) and machine current i_a (lower graph).

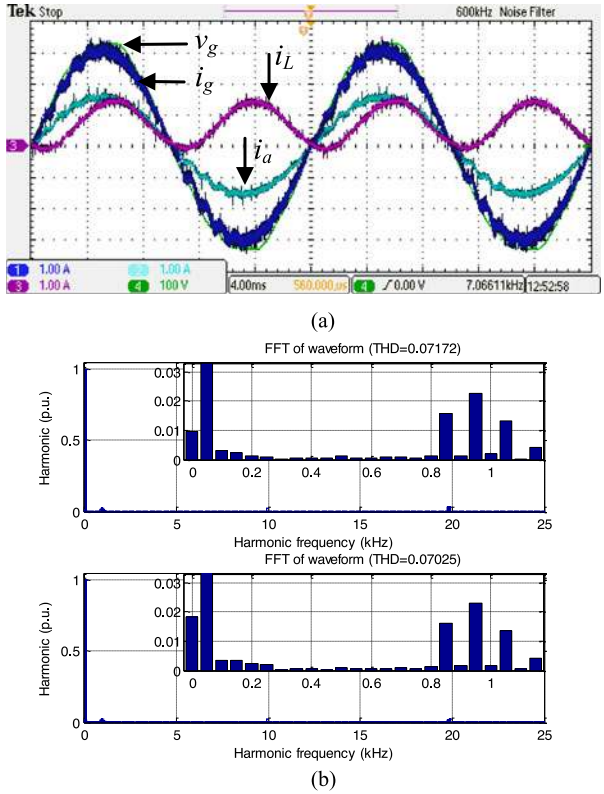

Fig. 11. Five-phase machine in charging mode: (a) grid voltage v_g, grid current i_g, machine current i_a, and battery charging current i_L; (b) spectra of grid current i_g (upper graph) and machine current i_a (lower graph).

meeting of grid standards and regulations, namely, a simple way of using interleaving strategy. Interleaving is a modulation strategy with which converter legs connected to the same grid terminal, and which have the same reference, are not switched simultaneously. Instead, carriers are shifted by 360° divided by the number of inverter legs sharing the same grid terminal. In the case of a nine-phase and a six-phase machine there are three inverter legs sharing a common grid terminal at each side. Thus, the phase shift between carriers is 120°. In the case of a five-phase machine, the positive grid terminal has two machine phases attached [see Fig. 1(c)], while the negative has three. Therefore, carriers of the first two phases are mutually shifted by 180°, while the mutual shift of carriers of the remaining three phases is 120°.

The same control algorithms (see Figs. 3–6), including current balancing and interleaving strategy, can be used for V2G operation. The only difference is that a minus sign should be placed in front of the reference for the grid current amplitude.

IV. Experimental Results

In order to verify the theoretical concepts and control, experiments are performed for the four discussed topologies. The experimental rig is given in Fig. 7, while the data are given in Appendix II. It should be noted that the utilized machines are all of induction type and are not optimized for vehicular applications. The grid is 240 V, 50 Hz. An amplifier, "Spitzenberger & Spies," is employed to emulate a battery and an optional dc–dc converter. DC-bus voltage is set to 600 V. A resistor of 0.5 Ω is placed between the amplifier and the inverter in order to emulate battery's internal resistance. The inverter operates at 10 kHz, with asymmetrical PWM; thus, the control frequency is 20 kHz. The dead time is 6 μs.

As already noted, an equivalent scheme and control of all four configurations is essentially the same (with the exception of the first set balancing of a five-phase machine). Therefore, in what follows experimental results are presented in parallel for the four topologies. This is particularly useful in order to observe influence of filter (i.e., machine phases) impedance on the charging/V2G process.

A. Charging Mode

Experimental results of the charging process are given in Figs. 8–11, for the asymmetrical nine-phase, the asymmetrical and symmetrical six-phase, and the five-phase machines, respectively. The grid current amplitude reference is set to 3 A. It is evident that all topologies perform charging at unity power factor, since grid currents are in phase with grid voltages. If grid currents are compared, it can be seen that although their amplitudes are the same, the ripple varies significantly. It is the highest in Fig. 10(a), which employs the symmetrical six-phase

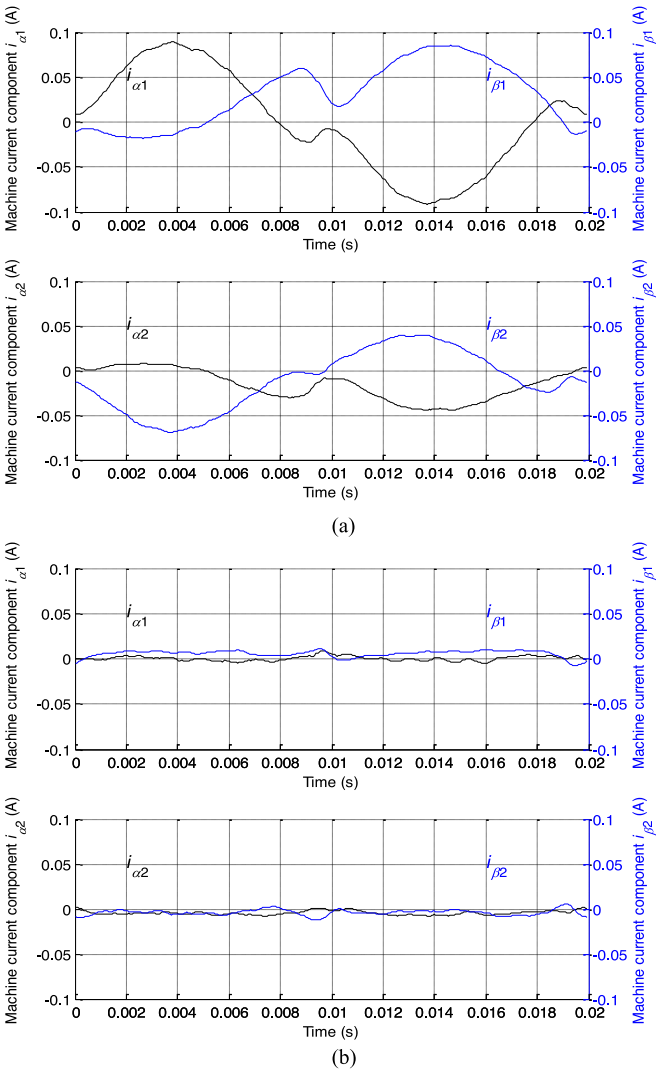

Fig. 12. Excitation of the α–β planes of the first and the second set of the nine-phase machine in the case when: (a) the current balancing is disabled and (b) the current balancing is enabled. Experimental data retrieved from dSpace.

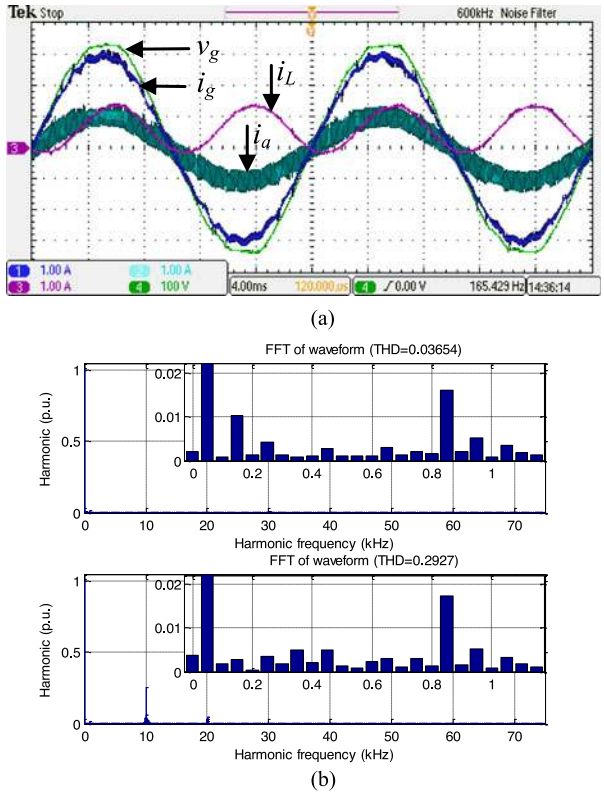

Fig. 13. Nine-phase machine in charging mode employing interleaving process: (a) grid voltage v_g, grid current i_g, machine current i_a, and battery charging current i_L; (b) spectra of grid current i_g (upper graph) and machine current i_a (lower graph).

machine, since its stator leakage inductance is three to five times smaller than in any other machine (see Appendix II). The other three machines have comparable stator leakage inductances; the five-phase one has the highest leakage inductance; thus, its grid current ripple is the lowest [see Fig. 11(a)]. However, from the grid current spectra of all machines, shown in upper parts of Figs. 8(b)–11(b), it can be seen that the difference is just in the switching ripple. They show no low-order harmonics of more than 0.5% of the fundamental. This is a result of proper operation of the current control algorithm (see Figs. 3 and 5), which manages control of the first 15 harmonics.

The same oscilloscope recordings include the machines' phase a currents i_a. It can be seen that they are in phase with grid currents. Moreover, the spectra, shown in Figs. 8(b)–11(b) below grid current spectra, exhibit great similarity with grid current spectra. This is an obvious consequence of the fact that the same currents flow through them, only scaled. In the case of asymmetrical nine-phase and asymmetrical and symmetrical six-phase machines, sets of three machine phases are paralleled together; thus, the machines' phase a currents i_a are three times lower than grid currents i_g, as is evident from the oscilloscope recordings. On the other hand, in the case of a five-phase machine, on one side three machine phases are paralleled, while on the other side, there are only two. This is why this machine's phase a current is only two times lower than the grid current i_g. If machine current ripple is examined, it can be seen that it is proportionally the same as the one of the grid current. Thus, again, the ripple of the symmetrical six-phase machine is the highest.

The effect of current balancing between paralleled machine phases is illustrated for the nine-phase machine in Fig. 12. Simple hard paralleling of phases gives excitation in the α–β plane of each set, as is obvious from Fig. 12(a) that is valid when current balancing control is disabled. This is a reflection of asymmetry between current sharing among the phases. On the other hand, when balancing control is turned on, the first harmonic gets zeroed, as is clear from Fig. 12(b). Now, the only current component of each set is the zero sequence, which represents grid current. Therefore, machine currents are balanced. Indeed, the rms values of the first set are now 0.7039, 0.7040, and 0.7041 A, in contrast to the values 0.7452, 0.6655, and 0.7023 A, which they have if current balancing control is switched off. In the

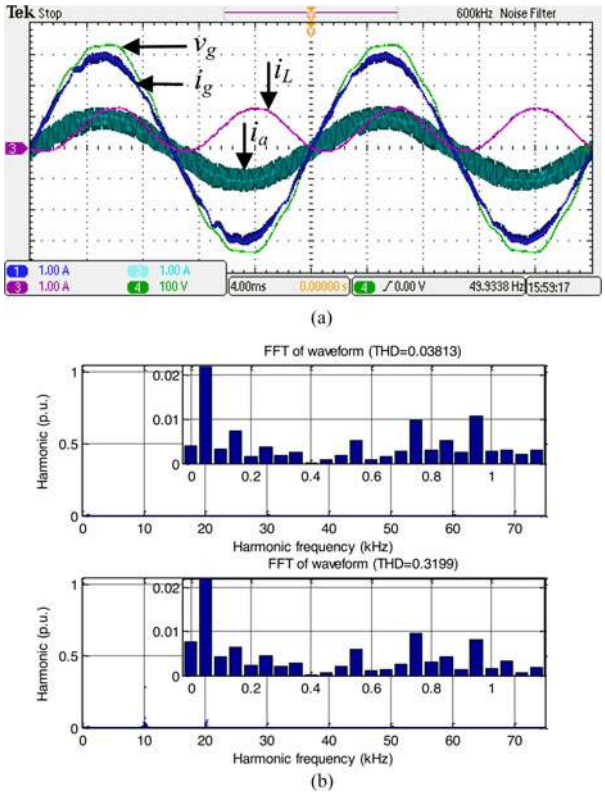

Fig. 14. Asymmetrical six-phase machine in charging mode employing interleaving process: (a) grid voltage v_g, grid current i_g, machine current i_a, and battery charging current i_L; (b) spectra of grid current i_g (upper graph) and machine current i_a (lower graph).

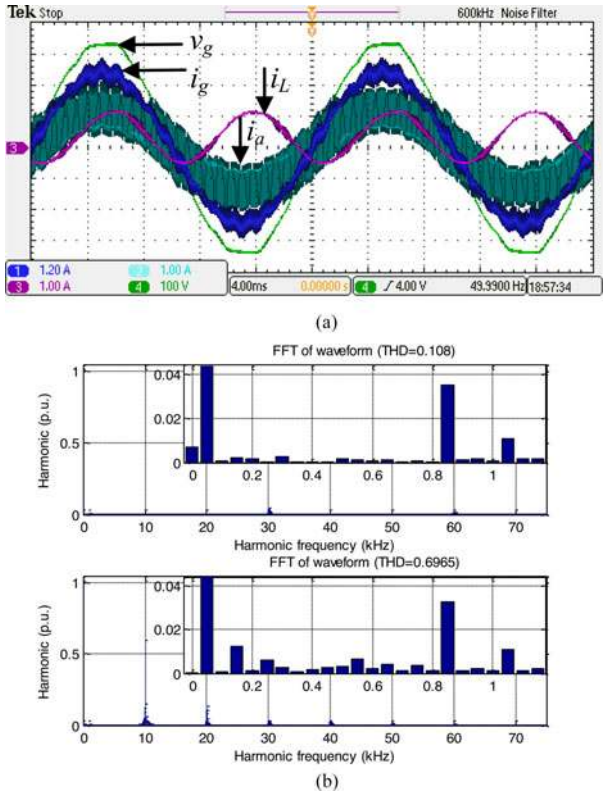

Fig. 15. Symmetrical six-phase machine in charging mode employing interleaving process: (a) grid voltage v_g, grid current i_g, machine current i_a, and battery charging current i_L; (b) spectra of grid current i_g (upper graph) and machine current i_a (lower graph).

case of all the other topologies, the α–β plane excitations are very similar; thus, in order to avoid repetition, they are omitted here.

The final trace in the oscilloscope recordings is the battery charging current. It is interesting to note that this current has the highest ripple in the case of a symmetrical six-phase machine. This is a direct consequence of the fact that input power ripple is the highest for this machine, which than reflects on the output power ripple, which is determined only by the battery charging current ripple. At instants when input power drops to zero, the battery is charged by the energy that is accumulated in the system. When that energy is utilized, the battery has to produce some power to cover the losses; thus, the charging current changes sign. This phenomenon is evident from oscilloscope recordings. However, the dc component of this current determines how long the charging will take place, and it can be seen that it has a significant value for all topologies.

B. Charging Mode Employing Interleaving Strategy

The effect of applying interleaving modulation strategy on the four studied topologies during the battery charging process is shown in Figs. 13–16. Since the operating conditions remained the same as for the process without the interleaving, a comparison can be made. At first, it is clear that grid current ripple reduced significantly in all topologies. This is obvious if Figs. 8–11 are compared to Figs. 13–16 in terms of the grid current total harmonic distortion (THD), the value of which is given just above the grid current spectra in these figures. It should also be noted that the absolute value of current switching ripple would not be significantly affected if the charging is performed at higher powers. Again, the symmetrical six-phase machine has the highest and the five-phase machine has the lowest grid current ripple. The reduction is a consequence of the fact that a major part of the machine's phase current ripple flows through other machine phases and does not penetrate the grid.

On the other hand, if machine currents are inspected, it can be seen that their ripples increase significantly. Switching harmonics can now circulate in the three paralleled phases (or two and three in the case of a five-phase machine), which was not the case when they had simultaneous carriers. The increase of the current ripple in all machines is around three times. It is important to note that a conclusion cannot be made about grid current ripple on the basis of the machine current ripple (as the case was when interleaving was not employed), since a major part of the ripple does not enter the grid. It should also be noted that the asymmetrical six-phase machine that is used in the experiment has different parameters in different planes [28], due to specifics of its design. Therefore, a somewhat modified interleaving strategy is employed, specifics of which are, however, beyond the scope of this paper.

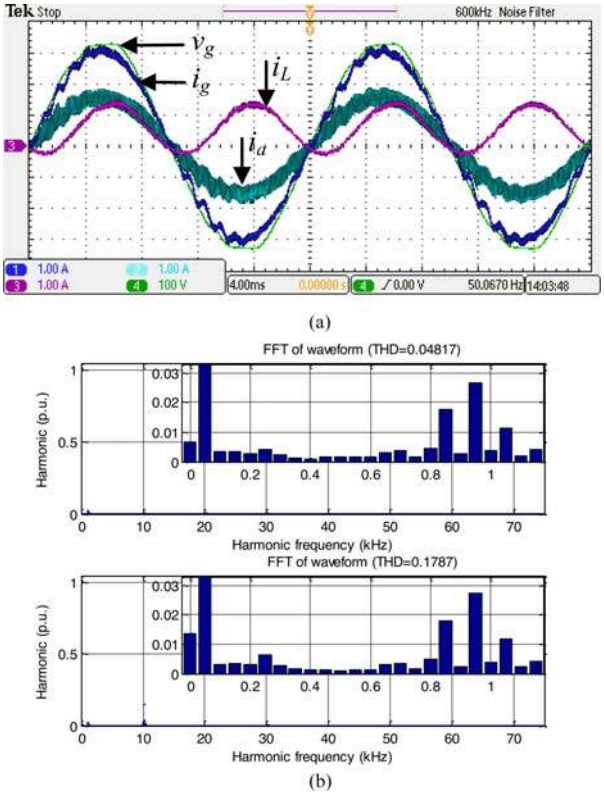

Fig. 16. Five-phase machine in charging mode employing interleaving process: (a) grid voltage v_g, grid current i_g, machine current i_a, and battery charging current i_L; (b) spectra of grid current i_g (upper graph) and machine current i_a (lower graph).

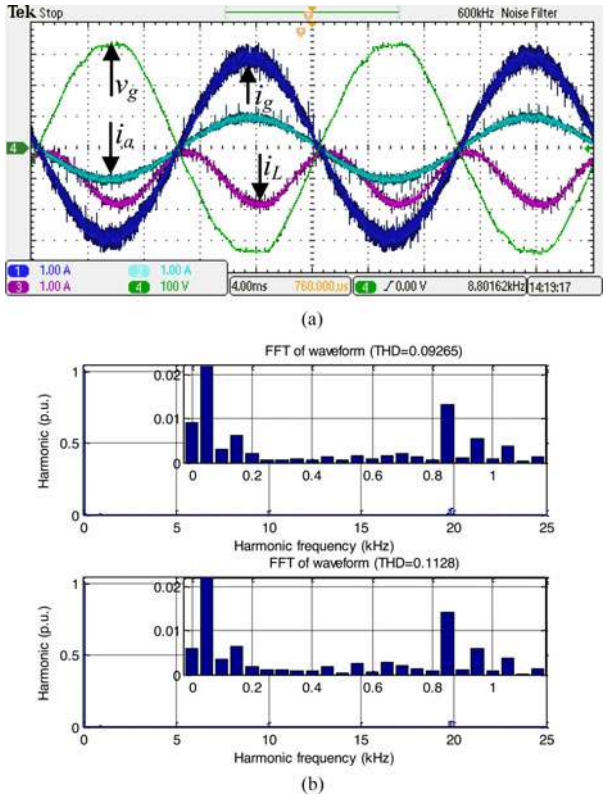

Fig. 17. Nine-phase machine in V2G mode: (a) grid voltage v_g, grid current i_g, machine current i_a, and battery charging current i_L; (b) spectra of grid current i_g (upper graph) and machine current i_a (lower graph).

Finally, some conclusions regarding the effect of interleaving process on charging efficiency can be drawn based on the battery charging current i_L. It can be seen that it has a lower ripple in all topologies. However, this current's dc value determines the charging power and, therefore, the efficiency. From oscilloscope traces, it can be seen that in the case of the asymmetrical nine-phase, asymmetrical six-phase, and five-phase machines, the value remains similar as before interleaving strategy was applied. Since in this case the interleaving strategy does not significantly influence the efficiency of the charging process, its utilization is recommended in order to comply with grid standards and regulations. However, in the case of the symmetrical six-phase machine, the dc value of the battery charging current is substantially reduced. Thus, a considerable part of energy that is taken from the grid is used to cover the losses in the machine's windings. Therefore, the interleaving strategy in this case should be avoided.

C. V2G Mode

The interleaving strategy has the same effect on V2G process as on the charging process. Therefore, in Figs. 17–20 experimental results of V2G operation are given only for the case when interleaving strategy is not employed. The current reference is set to -3 A, and the same four topologies are studied. Unity power factor operation is again obvious. If compared with

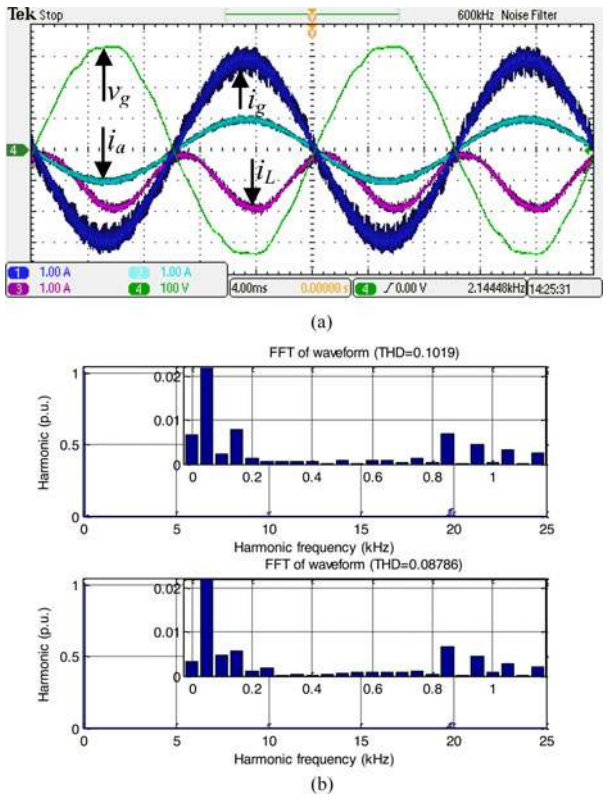

Fig. 18. Asymmetrical six-phase machine in V2G mode: (a) grid voltage v_g, grid current i_g, machine current i_a, and battery charging current i_L; (b) spectra of grid current i_g (upper graph) and machine current i_a (lower graph).

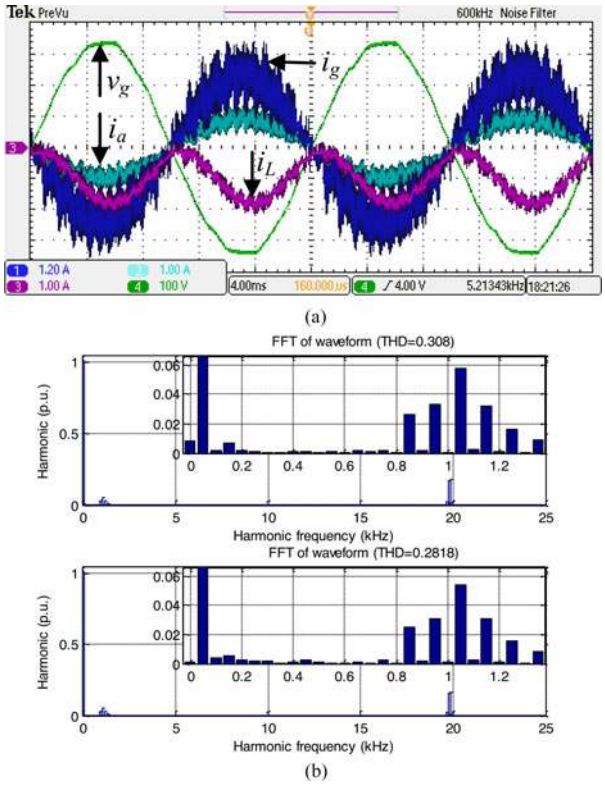

Fig. 19. Symmetrical six-phase machine in V2G mode: (a) grid voltage v_g, grid current i_g, machine current i_a, and battery charging current i_L; (b) spectra of grid current i_g (upper graph) and machine current i_a (lower graph).

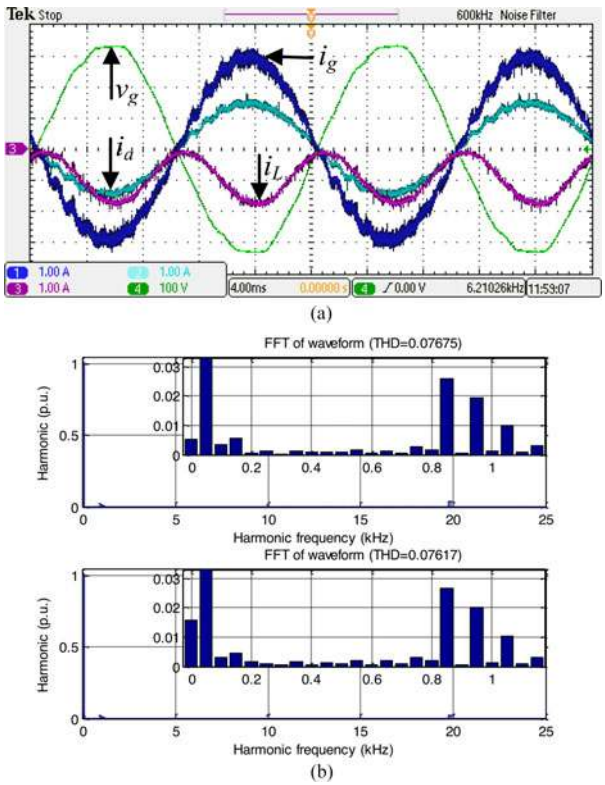

Fig. 20. Five-phase machine in V2G mode: (a) grid voltage v_g, grid current i_g, machine current i_a, and battery charging current i_L; (b) spectra of grid current i_g (upper graph) and machine current i_a (lower graph).

the charging mode (see Figs. 8–11), it can be seen that grid currents have almost the same ripple and spectrum; however they are now in phase opposition with the voltage. The same is valid for machines' currents. The only difference can be seen in the battery charging currents, since they do not change the sign during the operation. They are always negative. This is a consequence of the fact that, even when the output power, which gets injected into the grid, drops to zero, still some energy has to be provided from the battery to cover the losses, mostly on the filter. Therefore, the battery current never reaches zero value.

D. Transient From V2G Into Charging Mode

Finally, by changing the current reference from -3 to 3 A in a step-wise manner, a transient from V2G into the charging process is initiated. The obtained results are shown in Fig. 21. Although fast transient is not a major concern in vehicular charging applications, it is obvious that in all four topologies grid currents reach their references quickly. Some low-order harmonics appear during the transient. However, the energy flow almost instantly changes its direction as can be seen from the battery charging/discharging currents.

V. Preliminary Investigation of the Efficiency

Efficiency is considered as one of the crucial attributes of integrated chargers, and it can be estimated from the given experimental results. The battery power is $P_{\rm bat} = V_{\rm dc} I_L$, while the grid power is $P_g = V_g I_g$ (unity power factor operation at all times). The experimental results contain waveforms of battery charging current, grid voltage, and grid current, and the battery emulator dc voltage is 600 V in all cases. Using these data, it is possible to estimate the efficiency. Efficiencies in charging and V2G modes are assessed and compared. The results are given in Tables III and IV for the control of the systems without interleaving strategy. Below each value, a figure from which the value is obtained is indicated. It can be seen that the efficiencies of topologies in the charging mode are between 79% and 86%. In V2G mode, they are slightly higher, between 81% and 89%.

The obtained efficiencies are of course lower than one would hope for in a real-world scenario. However, the following caveats should be noted. All the machines used here are of very small power rating, so that stator winding resistances are inherently high. None of the machines has been designed specifically for vehicular applications. Three out of four were obtained by rewinding stator of a three-phase machine (the exception being the five-phase one, where new stator laminations with 40 slots were manufactured). Further, the power ratings of the machines are mutually different. Last but not least, the inverters used are not matched to the machines in terms of the power rating and are of much higher power. Thus the obtained efficiencies, typically over 80%, should only be taken as indicative. It is reasonable to expect that, with a multiphase machine optimized for vehicular applications and of substantially higher rated power, as well as with a converter that matches the machine's ratings, substantially higher efficiencies would result.

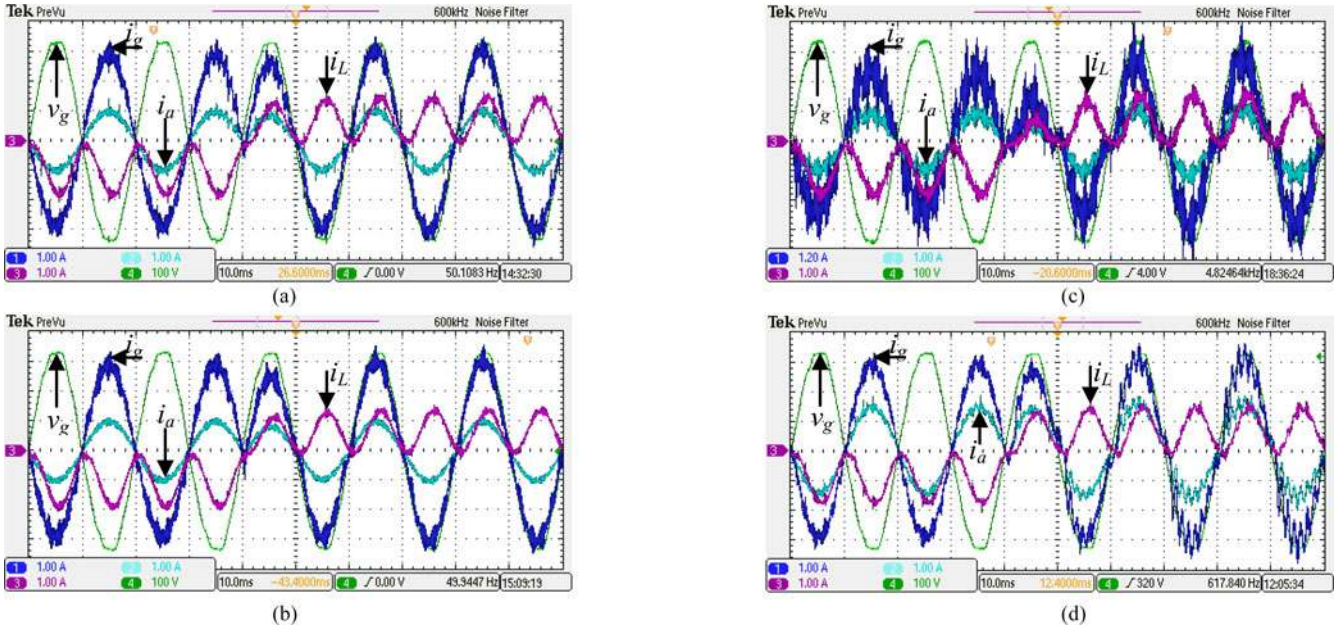

Fig. 21. Transient from V2G into charging mode of operation. Graphs depict grid voltage v_g, grid current i_g, machine current i_a, and battery charging current i_L. Results are given for the following machine types: (a) nine-phase, (b) asymmetrical six-phase, (c) symmetrical six-phase, and (d) five-phase.

TABLE III
CHARGING-MODE EFFICIENCIES

Topology	V_g (rms) (V)	I_g (rms) (A)	$V_{\rm dc}$ (V)	I_L (A)	Input power ($P_g = V_g I_g$) (W)	Output power ($P_{\rm bat} = V_{\rm dc} I_L$) (W)	Efficiency ($P_{\rm bat}/P_g$)
Nine-phase	240 (see Fig. 8)	2.13 (see Fig. 8)	600	0.73 (see Fig. 8)	510.7	439.4	0.86
Asymmetrical six-phase	240 (see Fig. 9)	2.13 (see Fig. 9)	600	0.67 (see Fig. 9)	510.7	404	0.79
Symmetrical six-phase	240 (see Fig. 10)	2.20 (see Fig. 10)	600	0.72 (see Fig. 10)	527.8	429.5	0.81
Five-phase	240 (see Fig. 11)	2.15 (see Fig. 11)	600	0.70 (see Fig. 11)	517	421.9	0.82

TABLE IV
V2G-MODE EFFICIENCIES

Topology	V_g (rms) (V)	I_g (rms) (A)	$V_{\rm dc}$ (V)	I_L (A)	Output power ($P_g = V_g I_g$) (W)	Input power ($P_{\rm bat} = \lvert V_{\rm dc} I_L \rvert$) (W)	Efficiency ($P_g/P_{\rm bat}$)
Nine-phase	240 (see Fig. 17)	2.06 (see Fig. 17)	600	−0.96 (see Fig. 17)	495.4	578.9	0.86
Asymmetrical six-phase	240 (see Fig. 18)	2.06 (see Fig. 18)	600	−1.01 (see Fig. 18)	493.9	605.4	0.82
Symmetrical six-phase	240 (see Fig. 19)	1.96 (see Fig. 19)	600	−0.97 (see Fig. 19)	470.6	583.7	0.81
Five-phase	240 (see Fig. 20)	2.08 (see Fig. 20)	600	−0.93 (see Fig. 20)	498	561.1	0.89

VI. CONCLUSION

The paper provides comprehensive analysis of single-phase battery chargers incorporating multiphase machines. One entirely novel topology, based on a five-phase machine, is proposed. A complete control algorithm, applicable to all investigated structures, is introduced next. The control includes machine current balancing algorithm.

All topologies are experimentally assessed in both charging and V2G mode in the laboratory conditions. The necessity of machine current balancing among machine sets is illustrated using experimental data and the improvement, obtained with the current balancing algorithm, is experimentally verified. The influence of interleaving modulation strategy on all studied machines is investigated and it is shown that, while interleaving always improves the grid current, deterioration in the machine's current waveform may overweigh the improvement of the grid current making interleaving undesirable.

All experiments are performed at unity power factor and, as demonstrated using experimentally obtained grid current

spectra, grid currents are almost completely free of low-order harmonics.

As noted already, battery charging integrated on-board solutions, developed and verified in this paper, enable slow charging and complement the corresponding fast charging solutions for the studied phase numbers, described in recent papers. Thus multiphase machines and power electronics offer means for realizing both slow and fast integrated on-board battery chargers with zero average torque development, with either no or with a minimum hardware reconfiguration.

Appendix I
Derivations of Equations from Section II

A derivation process of equations listed in Table II is given here. With derivations of all topologies' excitation mapping being similar to each other, it is sufficient to provide a derivation of a general case. A symmetrical six-phase topology is utilized for this purpose.

Decoupling matrix of symmetrical six-phase systems, given in [27], can be written in space vector form as

$$\underline{f}_{\alpha\beta} = \sqrt{2/6}\left(f_a + \underline{a}f_b + \underline{a}^2 f_c + \underline{a}^3 f_d + \underline{a}^4 f_e + \underline{a}^5 f_f\right) \quad \text{(A1)}$$

$$\underline{f}_{\mathrm{xy}} = \sqrt{2/6}\left(f_a + \underline{a}^2 f_b + \underline{a}^4 f_c + \underline{a}^6 f_d + \underline{a}^8 f_e + \underline{a}^{10} f_f\right). \quad \text{(A2)}$$

Here, $\underline{a} = \exp(j\delta) = \cos\delta + j\sin\delta$, where $\delta = 2\pi/6$, and f stands for any variable that is being transformed. From [27], the relevant zero-sequence components are given with

$$f_{0-} = \sqrt{1/6}\,(f_a - f_b + f_c - f_d + f_e - f_f) \quad \text{(A3)}$$

$$f_{0+} = \sqrt{1/6}(f_a + f_b + f_c + f_d + f_e + f_f). \quad \text{(A4)}$$

Substitution of the corresponding column of Table I [see Fig. 1(b)] into (A1) leads to the following expression:

$$\underline{i}_{\alpha\beta} = \sqrt{\frac{2}{6}} \cdot \left\{ \frac{i_{+g}}{3} + e^{j\frac{2\pi}{6}} \cdot \frac{i_{-g}}{3} + e^{j\frac{4\pi}{6}} \cdot \frac{i_{+g}}{3} + e^{j\frac{6\pi}{6}} \cdot \frac{i_{-g}}{3} + e^{j\frac{8\pi}{6}} \cdot \frac{i_{+g}}{3} + e^{j\frac{10\pi}{6}} \cdot \frac{i_{-g}}{3} \right\}. \quad \text{(A5)}$$

Grid currents can be taken in front of the brackets so that (A5) [by taking into consideration (1)] gives

$$\underline{i}_{\alpha\beta} = \sqrt{\frac{2}{6}} \cdot I \cdot \sqrt{2} \cdot \cos(\omega t) \cdot \frac{1}{3} \cdot \left\{ 1 - e^{j\frac{2\pi}{6}} + e^{j\frac{4\pi}{6}} - e^{j\frac{6\pi}{6}} + e^{j\frac{8\pi}{6}} - e^{j\frac{10\pi}{6}} \right\} = \sqrt{\frac{2}{6}} \cdot I \cdot \sqrt{2} \cdot \cos(\omega t) \cdot \frac{1}{3} \cdot 0 = 0. \quad \text{(A6)}$$

With the same type of derivation, excitation in the *x*--*y* plane can also be obtained as $\underline{i}_{\mathrm{xy}} = 0$. If zero sequence is considered, substitution of (1) and the corresponding column of Table I into (A3) gives

$$i_{0-} = \sqrt{\frac{1}{6}} \cdot \left\{ \frac{i_{+g}}{3} + \frac{i_{+g}}{3} + \frac{i_{+g}}{3} + \frac{i_{+g}}{3} + \frac{i_{+g}}{3} + \frac{i_{+g}}{3} \right\} = \sqrt{\frac{1}{6}} \cdot I \cdot \sqrt{2} \cdot \cos(\omega t) \cdot \frac{1}{3} \cdot 6 = \frac{\sqrt{12}}{3} \cdot I \cdot \cos(\omega t). \quad \text{(A7)}$$

In the same manner, the second zero-sequence component can be obtained as $i_{0+} = 0$. By employing derivation principles given here for the case of a symmetrical six-phase machine, values in Table II can be obtained for all the other considered topologies.

Appendix II
Machine and Other Data

DC sink/source: "Spitzenberger & Spies"—two DM 2500/PAS single-phase mains emulation systems are connected in series. An additional resistive load (RL 4000) is connected to the supply, enabling power sinking of up to 4 kW.

Controller: dSPACE DS1006 processor board. DS2004 high-speed A/D board is used for the A/D conversion of the measured machine currents and grid voltages. DS5101 Digital Waveform Output Board is used for the PWM.

Converters: Two two-level eight-phase inverters with EUPEC FS50R12KE3 IGBTs. Each has a continuous rating of approximately 28 kVA.

Asymmetrical nine-phase induction machine: 2.2 kW, 230 V (phase-to-neutral), 50 Hz, one pole pair, $R_s = 6.5\ \Omega, R_r = 1.3\ \Omega, L_{\gamma s} = 25$ mH, $L_{\gamma r} = 9$ mH, and $L_m = 1.3$ H.

Asymmetrical six-phase induction machine: 1.1 kW, $P = 3$, $R_s = 12.5\ \Omega, R_r = 6\ \Omega, L_{\gamma s} = 36$ mH, $L_{\gamma r} = 36$ mH, and $L_m = 0.6$ H.

Symmetrical six-phase induction machine: 1.1 kW, $P = 3$, $R_s = 3.6\ \Omega, R_r = 1.8\ \Omega, L_{\gamma s} = 8$ mH, $L_{\gamma r} = 11$ mH, $L_m = 0.2$ H.

Five-phase induction machine: Two pole pairs, $R_s = 2.9\ \Omega, R_r = 2.2\ \Omega, L_{\gamma s} = 43$ mH, $L_{\gamma r} = 17$ mH, and $L_m = 0.5$ H.

References

[1] J. Lee and B. Han, "A bidirectional wireless power transfer EV charger using self-resonant PWM," *IEEE Trans. Power Electron.*, vol. 30, no. 4, pp. 1784–1787, Apr. 2015.

[2] S. Y. Choi, J. Huh, W. Y. Lee, and C. T. Rim, "Asymmetric coil sets for wireless stationary EV chargers with large lateral tolerance by dominant field analysis," *IEEE Trans. Power Electron.*, vol. 29, no. 12, pp. 6406–6420, Dec. 2014.

[3] J. D. Santiago, H. Bernhoff, B. Ekergård, S. Eriksson, S. Ferhatovic, R. Waters, and M. Leijon, "Electrical motor drivelines in commercial all-electric vehicles: A review," *IEEE Trans. Veh. Technol.*, vol. 61, no. 2, pp. 475–484, Feb. 2012.

[4] S. Kinoshita, "Electric system of electric vehicle," U.S. Patent 5 629 603, 1997.

[5] C. Stancu, S. Hiti, and E. Mundt, "Mobile electric power for medium and heavy duty hybrid electric vehicles," in *Proc. IEEE Power Electron. Spec. Conf.*, Aachen, Germany, 2004, pp. 228–234.

[6] F. Lacressonniere and B. Cassoret, "Converter used as a battery charger and a motor speed controller in an industrial truck," presented at the Eur. Power Electron. Appl. Conf., Dresden, Germany, 2005.

[7] I. Subotic, N. Bodo, E. Levi, and M. Jones, "On-board integrated battery charger for EVs using an asymmetrical nine-phase machine," *IEEE Trans. Ind. Electron.*, vol. 62, no. 5, pp. 3285–3295, May 2015.

[8] S. Haghbin, S. Lundmark, M. Alakula, and O. Carlson, "Grid-connected integrated battery chargers in vehicle applications: Review and new solution," *IEEE Trans. Ind. Electron.*, vol. 60, no. 2, pp. 459–473, Feb. 2013.

[9] S. Haghbin and I. S. Guillen, "Integrated motor drive and non-isolated battery charger based on the torque cancelation in the motor," in *Proc. IEEE Int. Conf. Power Electron. Drive Syst.*, Kitakyushu, Japan, 2013, pp. 824–829.

[10] I. Subotic, N. Bodo, E. Levi, M. Jones, and V. Levi, "Isolated chargers for EVs incorporating six-phase machines," *IEEE Trans. Ind. Electron.*, vol. 63, no. 1, pp. 653–664, Jan. 2016.

[11] I. Subotic, E. Levi, and N. Bodo, "A fast on-board integrated battery charger for EVs using an asymmetrical six-phase machine," presented at the IEEE Vehicle Power Propulsion Conf., Coimbra, Portugal, 2014.
[12] I. Subotic, N. Bodo, and E. Levi, "An EV drive-train with integrated fast charging capability," *IEEE Trans. Power Electron.*, vol. 31, no. 2, pp. 1461–1471, Feb. 2016.
[13] L. De Sousa, B. Silvestre, and B. Bouchez, "A combined multiphase electric drive and fast battery charger for electric vehicles," presented at the IEEE Veh. Power Propulsion Conf., Lille, France, 2010.
[14] A. G. Cocconi and G. Calif, "Combined motor drive and battery recharge system," U.S. Patent 5 341 075, 1995.
[15] S. Seung-Ki and L. Sang-Joon, "An integral battery charger for four-wheel drive electric vehicle," *IEEE Trans. Ind. Appl.*, vol. 31, no. 5, pp. 1096–1099, Sept./Oct. 1995.
[16] L. Solero, "Nonconventional on-board charger for electric vehicle propulsion batteries," *IEEE Trans. Veh. Technol.*, vol. 50, no. 1, pp. 144–149, Jan. 2001.
[17] G. Pellegrino, E. Armando, and P. Guglielmi, "An integral battery charger with power factor correction for electric scooter," *IEEE Trans. Power Electron.*, vol. 25, no. 3, pp. 751–759, Mar. 2010.
[18] D. Woo, D. Joo, and B. Lee, "On the feasibility of integrated battery charger utilizing traction motor and inverter and plug-in hybrid electric vehicle," *IEEE Trans. Power Electron.*, vol. 30, no. 12, pp. 7270–7281, Dec. 2015.
[19] W. E. Rippel and A. G. Cocconi, "Integrated motor drive and recharge system," U.S. Patent 5 099 186 A, 1992.
[20] S. Lacroix, E. Laboure, and M. Hilairet, "An integrated fast battery charger for electric vehicle," presented at the IEEE Veh. Power Propulsion Conf., Lille, France, 2010.
[21] S. Haghbin, T. Thiringer, and O. Carlson, "An integrated split-phase dual-inverter permanent magnet motor drive and battery charger for grid-connected electric or hybrid vehicles," in *Proc. Int. Conf Elect. Mach.*, Marseille, France, 2012, pp. 1941–1947.
[22] T. Lixin and S. Gui-Jia, "Control scheme optimization for a low-cost, digitally-controlled charger for plug-in hybrid electric vehicles," in *Proc. IEEE Energy Convers. Congr. Expo.*, Atlanta, GA, USA, 2010, pp. 3604–3610.
[23] N. Bodo, I. Subotic, E. Levi, and M. Jones, "Single-phase on-board integrated battery charger based on a nine-phase machine," in *Proc. IEEE Ind. Electron. Soc. Conf.*, Dallas, TX, USA, 2014, pp. 3210–3216.
[24] A. Choudhury, P. Pillay, and S. S. Williamson, "Comparative analysis between two-level and three-level dc/ac electric vehicle traction inverters using a novel dc-link voltage balancing algorithm," *IEEE J. Emerg. Select. Topics Power Electron.*, vol. 2, no. 3, pp. 529–540, Sep. 2014.
[25] N. Sakr, D. Sadarnac, and A. Gascher, "A review of on-board integrated chargers for electric vehicles," presented at EPE Energy Convers. Congr. Expo. Europe, Lappeenranta, Finland, 2014.
[26] S. Liu, S. Hahlbeck, T. Schoenen, and K. Hameyer, "An integrated on-board charger with direct grid connection for battery electrical vehicle," in *Proc. Int. Symp. Power Electron. Elect. Drives Autom. Motion*, Sorrento, Italy, 2012, pp. 335–340.
[27] E. Levi, R. Bojoi, F. Profumo, H. A. Toliyat, and S. Williamson, "Multiphase induction motor drives—A technology status review," *IET Elect. Power Appl.*, vol. 1, no. 4, pp. 489–516, Jul. 2007.
[28] D. Hadiouche, H. Razik, and A. Rezzoug, "On the modeling and design of dual-stator windings to minimize circulating harmonic currents for VSI fed AC machines," *IEEE Trans. Ind. Appl.*, vol. 40, no. 2, pp. 506–515, Mar./Apr. 2004.

Ivan Subotic (S'12) received the Dipl.Ing. and M.Sc. degrees in electrical engineering from the University of Belgrade, Belgrade, Serbia, in 2010 and 2011, respectively, and the Ph.D. degree from the Liverpool John Moores University, Liverpool, U.K., in 2015.

His current research interests include power electronics, electric vehicles, and control of multiphase drive systems.

Nandor Bodo received the master's degree in power electronics from the Faculty of Technical Sciences, University of Novi Sad, Novi Sad, Serbia, in 2009, and the Ph.D. degree in electrical engineering from Liverpool John Moores University, Liverpool, U.K., in 2013.

He is currently a Postdoctoral Research Associate with the Liverpool John Moores University. His current research interests include power electronics and variable-speed drives.

Emil Levi (S'89–M'92–SM'99–F'09) received the M.Sc. and Ph.D. degrees in electrical engineering from the University of Belgrade, Belgrade, Yugoslavia, in 1986 and 1990, respectively.

From 1982 to 1992, he was with the Department of Electrical Engineering, University of Novi Sad. He joined Liverpool John Moores University, Liverpool, U.K., in May 1992, where he has been a Professor of Electric Machines and Drives since September 2000. He is currently the Editor-in-Chief of the *IET Electric Power Applications*.

Dr. Levi was a Co-Editor-in-Chief of the IEEE TRANSACTIONS ON INDUSTRIAL ELECTRONICS from 2009 to 2013 and is currently an Editor of the IEEE TRANSACTIONS ON ENERGY CONVERSION. He is the recipient of the Cyril Veinott award of the IEEE Power and Energy Society for 2009 and the Best Paper award of the IEEE TRANSACTIONS ON INDUSTRIAL ELECTRONICS for 2008. In 2014, he received the "Outstanding Achievement Award" from the European Power Electronics (EPE) Association.